Advances in Nano Research, *Vol. 19, No. 3 (2025) 209-224*
https://doi.org/10.12989/anr.2025.19.3.209

Poro-elastic buckling performance of tapered higher-order functionally graded cellular beams encased in nanocomposite layers

Zahra Khoddami Maraghi**[1†], Ehsan Arshid*[1†] and Abdelouahed Tounsi[2,3]

[1]*Faculty of Engineering, Mahallat Institute of Higher Education, Mahallat, Iran*
[2]*Department of Civil and Environmental Engineering, King Fahd University of Petroleum & Minerals, 31261 Dhahran, Eastern Province, Saudi Arabia*
[3]*Material and Hydrology Laboratory, University of Sidi Bel Abbes, Faculty of Technology, Civil Engineering Department, Algeria*

(*Received March 28, 2022, Revised August 21, 2025, Accepted August 22, 2025*)

Abstract. This study aims to investigate the elastic buckling behavior of tapered sandwich beams with functionally graded cellular cores and carbon nanotube–reinforced facesheets. The main objective is to clarify how tapering, porosity distribution, and nanocomposite reinforcement influence the critical buckling load, thereby providing insights useful for the design of lightweight and mechanically efficient structural components. To achieve this, stress transformations at specific angles are performed to accurately determine the effective material properties corresponding to different reinforcement patterns along the beam thickness. The governing equilibrium equations are derived using the virtual displacement principle and the variational method, and are solved numerically by means of the differential quadrature method. A comprehensive parametric study is conducted to evaluate the effects of geometric characteristics, porosity coefficient, porosity distribution patterns, carbon nanotube reinforcement, and transformation angle on the critical buckling loads. The results demonstrate that tapered beams generally exhibit reduced buckling resistance compared to beams of uniform thickness, and that improper distribution of reinforcements along the thickness can lead to significant deviations in buckling performance.

Keywords: carbon nanotubes reinforced composites; cellular structures; critical buckling loads; sandwich structures; tapered beams

1. Introduction

Sandwich structures, including sandwich beams, are a fascinating and widely used form of structural design that has garnered significant attention in engineering and material science. These structures are characterized by their unique composition, which typically includes a lightweight core sandwiched between two relatively thin, stiff facesheets. This arrangement creates a structure that combines high strength and rigidity with low weight, making it exceptionally advantageous in various applications (Patil *et al*. 2023, Sorokin *et al*. 2001). The concept of sandwich structures relies on the synergistic interaction between the core and the face sheets. The facesheets, often made from materials such as metals, composites, or polymers, are responsible for bearing tensile and compressive forces. In contrast, the core, which is usually composed of materials like foam, honeycomb, or balsa wood, provides shear rigidity and stability while maintaining a lightweight profile. This combination enables sandwich structures to achieve excellent performance metrics, including resistance to bending and buckling (Ait Atmane *et al*. 2017, Arshid *et al*. 2025, Arshid and Khoddami Maraghi 2025). Different types of sandwich structures have been developed to cater to specific requirements. The core can vary significantly in terms of material and geometry. For instance, honeycomb cores are frequently employed in aerospace and automotive applications due to their exceptional strength-to-weight ratio and energy absorption characteristics (Arshid *et al*. 2024, He and She 2024, Khorasani *et al*. 2021). Foam cores, on the other hand, are often preferred in marine and civil engineering applications, where resistance to water absorption and thermal insulation is required. Balsa wood cores, which are both natural and renewable, are utilized in wind turbine blades and other environmentally sensitive applications. Moreover, some designs incorporate truss or corrugated cores, which further enhance stiffness and load-bearing capabilities while maintaining a low weight (Öner *et al*. 2024, Rajendran *et al*. 2024, Sekban *et al*. 2025, Selvamani *et al*. 2024a, b, Turan *et al*. 2025).

The applications of sandwich structures are extensive and diverse, spanning multiple industries. In the aerospace sector, they are extensively utilized in the construction of aircraft fuselages, wings, and tail structures (Dawe and Yuan 2001, Sekban *et al*. 2024, Turan *et al*. 2023, Yaylacı *et al*. 2025). The ability to reduce weight without compromising strength is critical in these applications, as it directly impacts fuel efficiency and performance. Similarly, in the automotive industry, sandwich panels are employed in car bodies and interiors to improve crashworthiness and reduce overall vehicle weight. In marine engineering, sandwich

*Corresponding author, Ph.D.,
E-mail: e.arshid@mahallat.ac.ir; ehsanarshid@gmail.com
**Co-corresponding author, Ph.D.,
E-mail: z.khoddami@gmail.com
† These authors contributed equally to this work

ISSN: 2287-237X (Print), 2287-2388 (Online)

structures are used in ship hulls, decks, and bulkheads to enhance buoyancy and durability. Furthermore, they are found in architectural and civil engineering, where they serve as lightweight panels for walls, roofs, and floors, providing insulation and load-bearing functionality. The energy sector also benefits from sandwich structures, particularly in wind turbine blades, where their high stiffness and lightweight properties are crucial for efficient energy generation. The advantages of sandwich structures are numerous, making them a preferred choice in many applications. The weight reduction achieved by using lightweight cores contributes significantly to energy savings and improved performance, especially in transport and aerospace applications. The high stiffness-to-weight ratio ensures that these structures can withstand significant loads without excessive deformation. Additionally, their ability to absorb and dissipate energy makes them highly effective in impact resistance and vibration damping. Thermal and acoustic insulation properties can also be tailored by selecting appropriate core materials, which is particularly valuable in buildings and vehicles (Arshid *et al*. 2021, Van Quyen *et al*. 2021, Zenkour and El-Shahrany 2021). The fabrication of sandwich structures often involves advanced manufacturing techniques, including adhesive bonding, vacuum bagging, and autoclave processing. These methods ensure a strong bond between the face sheets and the core, which is essential for optimal performance. However, challenges such as delamination, core crushing, and face sheet wrinkling must be addressed through careful design and material selection. Innovations in materials and manufacturing processes continue to expand the potential of sandwich structures, enabling their use in increasingly demanding applications. In conclusion, sandwich structures, including sandwich/composite beams and plates, represent a remarkable innovation in structural engineering (Ferdosi and Khorramabadi 2025). Their unique composition and properties allow them to excel in a wide range of applications, from aerospace and automotive to marine and civil engineering. By leveraging the synergistic relationship between lightweight cores and stiff face sheets, these structures achieve an unparalleled combination of strength, stiffness, and lightweight properties. The ongoing development of new materials and manufacturing techniques ensures that sandwich structures will remain at the forefront of engineering design, meeting the evolving needs of various industries.

Tapered beams, characterized by their variable thickness along their length, are an essential structural element in engineering and architecture. These beams are distinguished by their ability to efficiently manage stress distribution and minimize material usage while maintaining or improving structural performance (Bakhshi Khaniki and Hosseini-Hashemi 2017, Kumar and Harsha 2022). The design of tapered beams involves a gradual change in thickness, which allows for an optimal balance between strength and weight. This structural innovation has been widely adopted across a range of applications due to its unique mechanical properties and versatility. The principle underlying tapered beams is rooted in the efficient distribution of material in response to varying stress levels along the beam's length. In many structural scenarios, such as cantilevers or simply supported beams, the bending moment is not uniform. By tapering the beam, material can be concentrated in areas of higher stress, such as near supports or points of maximum moment, while reducing material in regions subjected to lower stress. This approach not only enhances the overall performance of the structure but also contributes to significant material savings, which is particularly important in cost-sensitive or resource-constrained applications. Tapered beams find extensive use in various industries and structural systems. In civil engineering, they are commonly employed in bridges, roof structures, and other large-span systems. The ability to reduce weight while maintaining strength is particularly advantageous in long-span applications, where self-weight contributes significantly to the overall loading. In the aerospace industry, tapered beams are integrated into aircraft wings and fuselage structures to optimize performance and reduce fuel consumption (Tang *et al*. 2025, Yao *et al*. 2024). The gradual transition in thickness allows for better aerodynamic performance and improved load-carrying capacity. Similarly, in the automotive sector, tapered beams are utilized in vehicle frames and chassis to enhance crashworthiness and improve energy absorption during impacts. Architectural design also benefits significantly from the use of tapered beams, where their aesthetic appeal complements their structural efficiency. The sleek and elegant profile of these beams allows for innovative and visually striking designs, particularly in modern buildings and open spaces. In addition to their structural and aesthetic benefits, tapered beams are often used in wind turbines and offshore structures, where their ability to withstand dynamic loads and reduce material usage contributes to enhanced sustainability and reduced environmental impact. The advantages of tapered beams extend beyond their weight reduction and strength optimization (Arshid *et al*. 2025, Attia and Mohamed 2020). Their unique geometry allows for improved resistance to buckling and increased stability, particularly in slender or long-span structures. This makes them particularly suitable for applications where stability is critical, such as high-rise buildings and tall towers. Additionally, tapered beams offer improved energy dissipation properties, which can be leveraged in seismic design to enhance the resilience of structures subjected to dynamic loads. The fabrication of tapered beams often involves advanced manufacturing techniques, including extrusion, welding, and additive manufacturing. Modern technologies, such as computer-aided design (CAD) and finite element analysis (FEA), enable precise modeling and optimization of tapered beam geometry, ensuring that performance requirements are met while minimizing material waste. However, challenges such as stress concentration at transition points and potential fabrication complexities must be carefully addressed through meticulous design and quality control. The versatility of tapered beams also extends to their use in composite structures, where materials with different properties can be combined to achieve even greater performance benefits. For instance, tapered beams with composite face sheets and lightweight cores can be used to create sandwich structures that

combine the advantages of both tapered geometry and composite materials. These hybrid designs further enhance the potential applications of tapered beams, making them indispensable in advanced engineering and design. In brief, tapered beams represent a remarkable advancement in structural engineering, offering a blend of efficiency, strength, and versatility that is unmatched by uniform beams. Their ability to adapt to varying stress distributions and reduce material usage makes them a sustainable and cost-effective choice for a wide range of applications. As manufacturing technologies and design tools continue to evolve, the potential of tapered beams will only expand, enabling their use in increasingly complex and demanding structural systems. Their contribution to modern engineering and architecture is not only practical but also inspiring, demonstrating the power of innovation in transforming how materials and structures are utilized.

Functionally graded cellular materials (FGCMs) and nanocomposite materials, particularly those reinforced with carbon nanotubes (CNTs), represent cutting-edge advancements in material science (Alian *et al*. 2016, Cho 2024, Cui *et al*. 2024, Eltaher *et al*. 2024, Liu *et al*. 2024). These materials have revolutionized various industries by combining exceptional mechanical, thermal, and functional properties with tailored performance characteristics (Banhart 2001, Hajmohammad *et al*. 2018, Mirjavadi *et al*. 2020, Singh and Azam 2021). FGCMs are a class of materials in which the porosity varies gradually along one or more dimensions. This variation allows for the optimization of properties such as stiffness, strength, thermal conductivity, and permeability to meet specific application requirements. The gradual change in porosity is often achieved by varying the density or size of the pores within the material. This unique structure enables FGCMs to address challenges that conventional homogeneous materials cannot solve. For example, in biomedical engineering, these materials are utilized for implants and prosthetics, where a gradient in porosity allows for enhanced integration with surrounding tissues. The outer layers can mimic the dense structure of bone for load-bearing purposes, while the inner porous regions promote cell growth and nutrient exchange. This functional gradation not only improves biocompatibility but also reduces the risk of implant rejection. In thermal and acoustic insulation, FGCMs have found significant applications (Ninh *et al*. 2023). Their ability to provide varying levels of insulation across a single structure makes them invaluable in industries such as aerospace and automotive engineering. In these applications, the combination of lightweight properties and tailored thermal resistance contributes to improved energy efficiency and noise reduction. Moreover, the use of FGCMs in energy absorption systems, such as crashworthy components in vehicles or protective gear, has been extensively explored. The gradient in porosity enables these materials to dissipate energy effectively, enhancing safety and durability (Niu *et al*. 2025, Ren *et al*. 2025).

Nanocomposite materials, particularly those reinforced with CNTs, have emerged as a transformative class of materials due to their exceptional properties. CNTs, with their unique cylindrical nanostructure and extraordinary mechanical, thermal, and electrical properties, serve as an ideal reinforcement material (Moradi-Dastjerdi *et al*. 2020). When incorporated into a matrix, such as polymer, metal, or ceramic, CNTs significantly enhance the composite's overall performance. The high aspect ratio and strength of CNTs enable nanocomposites to exhibit remarkable stiffness, tensile strength, and toughness, even at low reinforcement concentrations. The applications of CNT-reinforced nanocomposites are diverse and impactful (Djilali *et al*. 2022, Ebrahimi 2019, Kiarasi *et al*. 2021, Matouk *et al*. 2020, Xia *et al*. 2023). In aerospace engineering, these materials are employed in structural components where weight reduction and superior mechanical properties are critical. The incorporation of CNTs in aircraft and spacecraft structures has improved fuel efficiency and performance while maintaining safety standards. Similarly, in the automotive industry, CNT-reinforced nanocomposites are utilized in components such as engine parts, body panels, and tires. These materials enhance durability, reduce weight, and improve thermal management, contributing to overall vehicle performance and sustainability. In the field of electronics, CNT-reinforced nanocomposites have played a pivotal role in developing advanced devices. Their exceptional electrical conductivity and thermal stability make them suitable for applications in sensors, flexible electronics, and high-performance batteries. For instance, CNT-reinforced polymers are used as conductive fillers in flexible circuits, enabling the production of lightweight, portable, and efficient electronic devices. Additionally, in energy storage, these nanocomposites are employed in electrodes for lithium-ion batteries and supercapacitors, where their high conductivity and surface area enhance energy density and charge-discharge rates. Biomedical applications of CNT-reinforced nanocomposites have also gained significant attention. These materials are used in drug delivery systems, where CNTs act as carriers for targeted therapy due to their high surface area and biocompatibility. Furthermore, in tissue engineering, CNT-reinforced scaffolds provide a conducive environment for cell growth and differentiation, enabling the regeneration of damaged tissues. Their ability to mimic the mechanical and structural properties of natural tissues makes them highly effective in these applications. The advantages of FGCMs and CNT-reinforced nanocomposites are numerous and far-reaching. The tailored properties of FG porous materials enable them to address specific challenges in load distribution, thermal management, and energy absorption. Meanwhile, CNT-reinforced nanocomposites offer unparalleled enhancements in mechanical, thermal, and electrical properties, paving the way for innovations across multiple industries. Despite these advantages, challenges such as the uniform dispersion of CNTs within the matrix and the optimization of manufacturing processes must be addressed to fully realize their potential. Advances in processing techniques, such as functionalization of CNTs and advanced fabrication methods, continue to push the boundaries of what these materials can achieve. FGCMs and CNT-reinforced nanocomposites represent a significant leap forward in mechanical, civil, and materials engineering. Their ability to combine exceptional properties with tailored performance characteristics has enabled their widespread

adoption in critical industries, including aerospace, automotive, electronics, and biomedicine. As research and development continue to advance, the potential applications and benefits of these materials are expected to grow, further transforming the landscape of modern engineering and technology. Consequently, numerous publications have emerged regarding the architectures of FGCMs (Abazid *et al*. 2020, Arshid *et al*. 2023, Bekkaye *et al*. 2020, Thang *et al*. 2018). Additionally, several studies (Khoddami Maraghi *et al*. 2022, Rasooli Jazi *et al*. 2024) examined sandwich constructions built of various materials, including the aforementioned nanocomposite and FGCMs (Babaei *et al*. 2024, Kaveh *et al*. 2024).

The structural configuration studied in this work is of considerable practical importance in advanced engineering. Tapered beams with functionally graded cellular cores and nanocomposite-reinforced facesheets are widely used in aerospace and civil engineering to achieve lightweight designs with improved buckling resistance, in marine and offshore structures to withstand demanding compressive environments, and in automotive applications where enhanced strength-to-weight ratios are critical (Liu *et al*. 2025, Ma and Liu 2025, Sun *et al*. 2025, Wang *et al*. 2025). Clarifying the buckling response of such beams under varying porosity distributions and reinforcement patterns provides design insights that are directly useful for the development of next-generation lightweight and stable structural components (Cao *et al*. 2025a, b, Cen *et al*. 2025, Meng *et al*. 2025).

Researchers have identified a deficiency in the literature regarding sandwich beams with FGCMs as the core and variable thicknesses after reviewing a large body of academic literature. In addition, these beams are enhanced by nanocomposite layers that are reinforced with CNTs. This finding has led them down a new line of inquiry, and they will be studying how different geometric factors and materials affect the elastic buckling properties of tapered beams supported on an elastic base. The authors have chosen to explain the displacement components of the model using the higher-order theory, which is known for its greater accuracy. Using generalized differential quadrature method (GDQM), the researchers were able to systematically evaluate the effects of various parameters on the structure's critical buckling loads after obtaining the equilibrium equations via the virtual displacement principle. Improving the creation of high-performance, more practical structural designs was their primary objective. Their study's findings will serve as a solid foundation for such investigations in the future.

2. Mathematical equations

Consider a variable thickness beam as consisting of three layers: the middle layer is built using an FGC structure, and the exterior layers are composed of polymers reinforced with CNTs. These layers are densely packed and usually do not separate from each other. In the upper layer, t_u stands for thickness, in the middle layer, $t(x)$ for thickness, and in the lower layer, t_l. The formula $t(x) = t_0(1 - \lambda x/a)$ is used to analyze variations in the thickness

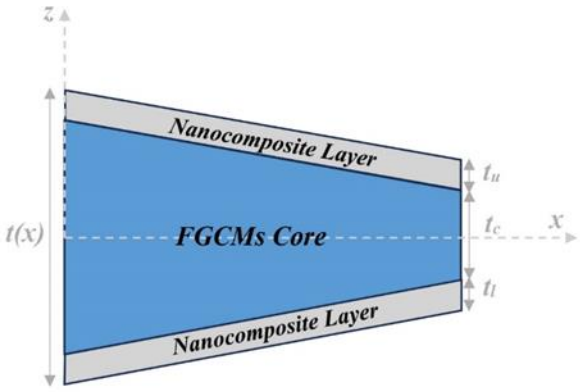

Fig. 1 Schematics of the under-consideration FGCM tapered beam with nanocomposite layers

of the beam's core. The length of the beam is represented by a, the beginning thickness by t_0, and the variations in form along the thickness direction by λ. In Fig. 1 we can see the model's schematics. Prior to establishing the kinematic relations, we shall examine the constitutive relations for the core and facesheets. Finally, the solution process and the findings will be described.

For the both core and facesheets, the following constitutive law is examined (Tahir *et al*. 2021):

$$\sigma_{ij}^{c,f} = C_{ijkl}^{c,f}(z)\varepsilon_{kl} \tag{1}$$

Here, the superscript c, f denotes the core and facesheets (f=t, l) and $C_{ijkl}^{c,f}(z)$ are the modified stiffness matrix components that for the core can be achieved using the below relations (Mousavi *et al*. 2021):

$$\begin{aligned} C_{11}^{c}(z) &= {E_c(z)}\big/{(1-\nu_c^2(z))}, \\ C_{55}^{c}(z) &= {E_c(z)}\big/{(2(1+\nu_c(z)))} \end{aligned} \tag{2}$$

In the given equations, ν_c represents Poisson's ratio and E_c represents Young's modulus. A lighter structure achieved by utilizing FGCMs is the declared goal of the current model's core architecture. Core porosity distribution is the primary determinant of elastic property changes. The structure of FGC cores determines their elastic characteristics. If the pores are symmetrically placed in the FGC core, therefore, the below relation apply to changes of its Young's elasticity modulus (Panah *et al*. 2019):

$$E_c(z) = E_0(1-e_0)\cos\left({\pi z}/{t(x)}\right) \tag{3}$$

The porosity coefficient, abbreviated as e_0, is the ratio of the volume of the material's pores to its overall volume. In contrast, a non-symmetric porous core has an uneven distribution of pores throughout its thickness. A rundown of the essential features is as follows:

$$E_c(z) = E_0(1-e_0)\cos\left({\pi z}/{2t(x)} + {\pi}/{4}\right) \tag{4}$$

Elastic modulus is thickness-independent parameter when the pores are uniformly distributed across the core's thickness:

$$E_c = E_0(1-\omega) \tag{5}$$

In which $\omega = 1-[(2\sqrt{1-e_0}-2)/(\pi+1)]^2$.

The attention now shifts to the elements of the stiffness matrix that comprise the facesheets. Given that the facesheets are not in an axial orientation, the modified stiffness components with respect to the rotational degree can be derived from the standard stiffness components ($Q^f_{ijkl}(z)$) (Khoddami Maraghi and Arshid, 2024):

$$C^f_{11}(z) = Q^f_{11}(z)cos^4(\theta) + 4Q^f_{55}(z)sin^2(\theta)cos^2(\theta), \tag{6}$$

$$C^f_{55}(z) = \left[Q^f_{11}(z) - 2Q^f_{55}(z)\right]sin^2(\theta)cos^2(\theta) + Q^f_{55}(z)[sin^4(\theta)+cos^4(\theta)] \tag{7}$$

In which θ=θ_1 and θ_2 are for the upper and lower facesheets, respectively. The ordinary stiffness components used for the facesheets may be obtained using the following relations:

$$\begin{aligned} Q^f_{11}(z) &= {E_{11}}/{(1-\nu_{12}\nu_{21})}, \\ Q^f_{55}(z) &= G_{12} \end{aligned} \tag{8}$$

Here, we use the extended rule of mixture scheme to determine the facesheets' material's qualities. Consequently, the shear and normal elasticity moduli are found to be (M. Babaei *et al*. 2022):

$$\begin{aligned} E_{11} &= \gamma_1 VF_{CNT}E^{CNT}_{11} + VF_mE_m, \\ {\gamma_3}/{G_{12}} &= {VF_{CNT}}/{G^{CNT}_{12}} + {VF_m}/{G_m} \end{aligned} \tag{9}$$

Here, VF_m stands for the matrix material percentage and VF_{CNT} for the CNTs proportion in the composite. The shear modulus, E^{CNT}_{11}, G^{CNT}_{12}, E_m, and G_m are the corresponding longitudinal and transverse Young's moduli and matrix components, respectively. Two efficiency metrics, specific to CNTs, are γ_1 and γ_3. Nevertheless, the facesheets' Poisson's ratio remains constant regardless of the CNT dispersion pattern and may be calculated using a specific formula in the following way:

$$\nu_{12} = VF^*_{CNT}\nu^{CNT}_{12} + VF_m\nu_m \tag{10}$$

By delving into different patterns of CNT dispersion, this study introduces the following functions:

$$VF^i_{CNT} = \begin{cases} VF^*_{CNT} & \text{U} \\ VF^*_{CNT}\times\left[1-\dfrac{2T}{t_i}\right] & \text{FG A} \\ VF^*_{CNT}\times\left[1+\dfrac{2T}{t_i}\right] & \text{FG V} \\ VF^*_{CNT}\times 2\left[1-\dfrac{2T}{t_i}\right] & \text{FG O} \\ VF^*_{CNT}\times\dfrac{4|T|}{t_i} & \text{FG X} \end{cases} \tag{11}$$

In which $T = z \mp (t_c+t_i)/2$, and i denotes to upper and lower facesheets. The formula for the volume fraction of carbon nanotubes, denoted as VF^*_{CNT}, is as follows:

$$VF^*_{CNT} = {w_{CNT}}\Big/{\left[w_{CNT} + \left({\rho_{CNT}}/{\rho_m}\right) - \left({\rho_{CNT}}/{\rho_m}\right)w_{CNT}\right]} \tag{12}$$

In this context, w_{CNT} is used to represent the mass percentage of CNTs, while ρ_m and ρ_{CNT} are used to represent the densities of the matrix and CNTs, respectively.

It now shifts its focus to studying the kinematic relations. Thus, it is necessary to specify the displacements of the tapering beam. Let us pretend that the structure's x- and z-axis displacements are denoted by u_1 and u_3, respectively. Thus, it is essential to initially define them according to the relations given below (Moradi-Dastjerdi and Behdinan, 2021):

$$\begin{aligned} u_1(x,z,t) &= u(x,t) - \chi(z)w(x,t)_{,x} + \phi(z)\psi(x,t), \\ u_3(x,z,t) &= w(x,t) \end{aligned} \tag{13}$$

Keep in mind that ψ represents the rotation of the mid-plane around the x-axis. When studying the distribution of stresses in the thickness direction, the effects of shear deformation are taken into consideration using the functions $\chi(z)$ and $\phi(z)$. Here they can be demonstrated within the framework of theory of higher-order shear deformation:

$$\chi(z) = z, \qquad \phi(z) = z\left(1-\frac{4z^2}{3t^2}\right) \tag{14}$$

To get the strain components, one can apply the following relations:

$$\varepsilon_{xx} = u_{1,x}, \qquad \gamma_{xz} = u_{1,z} + u_{3,x} \tag{15}$$

The equilibrium equations are simplified by applying the virtual displacement concept (Soleimani-Javid *et al*. 2021):

$$\delta(U_s - W_e) = 0 \tag{16}$$

The strain energy is introduced as U_s in Eq. (16), and W_e is the work done by external loads.

Step one is to look at the strain energy and how it changes. An expression for the strain energy associated with each layer of the three-layered beam looks like this (Shariati *et al*. 2020):

$$U_s = \frac{1}{2}\int_A \int_{-t(x)/2-t_l}^{+t(x)/2+t_u} [\sigma_{xx}\varepsilon_{xx} + \tau_{xz}\gamma_{xz}]\ \mathrm{d}z\ \mathrm{d}A \tag{17}$$

This allows us to rewrite the formula for variations in strain energy as follows:

$$\delta U_s = \int_A \left\{\left(-N_{xx,x}\right)\delta u - \left(M_{xx,xx}\right)\delta w + \left(Q_x - R_{xx,x}\right)\delta\psi\right\}\mathrm{d}A \tag{18}$$

in which:

$$\begin{Bmatrix} N_{xx} \\ M_{xx} \\ R_{xx} \end{Bmatrix} = \int_z \sigma_{xx}\begin{Bmatrix} 1 \\ \chi(z) \\ \phi(z) \end{Bmatrix}\mathrm{d}z, \qquad Q_x = \int_z \sigma_{xz}\,\mathrm{d}z \tag{19}$$

Besides resting on an elastic base that is represented by the Kerr model, the framework is also subjected to an in-plane mechanical load, as previously stated. This relation can be used to calculate the work of the imposed in-plane load:

$$W_{ip} = \frac{1}{2}\int_A \left[N^{ip}\left(w_{,x}\right)^2\right] \text{ dA} \tag{20}$$

in which N^{ip} is the applied in-plane load.

What follows is an examination of the Kerr model's application to the elastic foundation, which requires three parameters. The three factors that make up this model are the shear layer (K_s), the springs in the upper layer (K_u), and the springs in the lower layer (K_l). The following results are obtained by following this procedure in order to determine the work derivable from the Kerr foundation (Eghbali and Hosseini 2024, Karami and Shahsavari 2019, Shen *et al*. 2024):

$$W_f = \frac{1}{2}\int_A \left[-\left(\frac{K_l K_u}{K_l + K_u}\right)w + \left(\frac{K_s K_u}{K_l + K_u}\right)w_{,xx}\right]w \text{ dA} \tag{21}$$

Normal and shear stresses are both capable of withstanding this specific elastic base. Two layers of shear and a row of springs make it up. Thus, by adding W_{ip} and W_f, the total works applicable to the structure are obtained.

The following displacement-related equilibrium equations can be derived by substituting the resulting strain energy and external work formulae into the virtual displacement principle:

δu:

$$\begin{aligned}&(\alpha_1)u_{,xx} + \left(\frac{\mathrm{d}\alpha_1}{\mathrm{d}x}\right)u_{,x} - (\alpha_2)w_{,xxx} - \left(\frac{\mathrm{d}\alpha_2}{\mathrm{d}x}\right)w_{,xx}\\ &+\alpha_3\psi_{,xx} + \left(\frac{\mathrm{d}\alpha_3}{\mathrm{d}x}\right)\psi_{,x}\end{aligned} \tag{22}$$

δw:

$$\begin{aligned}&(\alpha_2)u_{,xxx} + 2\left(\frac{\mathrm{d}\alpha_2}{\mathrm{d}x}\right)u_{,xx} + \left(\frac{\mathrm{d}^2\alpha_2}{\mathrm{d}x^2}\right)u_{,x} - (\alpha_4)w_{,xxxx}\\ &-2\left(\frac{\mathrm{d}\alpha_4}{\mathrm{d}x}\right)w_{,xxx} - \left(\frac{d^2\alpha_4}{dx^2} + \frac{K_s K_u}{K_l + K_u} - N^{ip}\right)w_{,xx}\\ &+\left(\frac{K_l K_u}{K_l + K_u}\right)w + (\alpha_5)\psi_{,xxx} + 2\left(\frac{\mathrm{d}\alpha_5}{\mathrm{d}x}\right)\psi_{,xx}\\ &+\left(\frac{\mathrm{d}^2\alpha_5}{\mathrm{d}x^2}\right)\psi_{,x} = 0,\end{aligned} \tag{23}$$

$\delta\psi$:

$$\begin{aligned}&(\alpha_3)u_{,xx} + \left(\frac{\mathrm{d}\alpha_3}{\mathrm{d}x}\right)u_{,x} - (\alpha_5)w_{,xxx} - \left(\frac{\mathrm{d}\alpha_5}{\mathrm{d}x}\right)w_{,xx}\\ &+(\alpha_6)\psi_{,xx} + \left(\frac{\mathrm{d}\alpha_6}{\mathrm{d}x}\right)\psi_{,x} - (\alpha_7)\psi\end{aligned} \tag{24}$$

In which:

$$\begin{aligned}\alpha_1 &= \beta_1 + \beta_{17} + \beta_{33} + 4\beta_7 + 4\beta_{23},\\ \alpha_2 &= \beta_2 + \beta_{18} + \beta_{34} + 4\beta_8 + 4\beta_{24},\\ \alpha_3 &= \beta_4 + \beta_{20} + \beta_{36} + 4\beta_{10} + 4\beta_{26},\\ \alpha_4 &= \beta_3 + \beta_{19} + \beta_{35} + 4\beta_9 + 4\beta_{25},\\ \alpha_5 &= \beta_5 + \beta_{21} + \beta_{37} + 4\beta_{11} + 4\beta_{27},\end{aligned} \tag{25}$$

$$\begin{aligned}\alpha_6 &= \beta_6 + \beta_{22} + \beta_{38} + 4\beta_{12} + 4\beta_{28},\\ \alpha_7 &= \beta_{13} + \beta_{15} + \beta_{16} + \beta_{29} + \beta_{31} + \beta_{32}\\ &+\beta_{39} + 2\beta_{14} + 2\beta_{30}\end{aligned}$$

The associated boundary conditions must now be ascertained. Two different types of boundaries are considered for each end of the under-evaluation beam. The following relations are governed under clamped conditions:

$$u = w = \psi = w_{,x} = 0 \tag{26}$$

And for simply-supported conditions:

$$N_{xx} = w = \psi = M_{xx} = 0 \tag{27}$$

The following are the coefficients that are introduced for use in the equilibrium equations and boundary conditions:

$$\begin{aligned}&[\beta_1,\ \beta_2,\ \beta_3,\ \beta_4]\\ &= \int_{+t(x)/2-t_u}^{+t(x)/2} C_{11}^u \cos^4\theta_1 [1,\ \chi(z),\ \chi(z)^2,\ \phi(z)]\mathrm{d}z,\end{aligned} \tag{28}$$

$$[\beta_5,\ \beta_6] = \int_{+t(x)/2-t_u}^{+t(x)/2} C_{11}^u \cos^4\theta_1 [\chi(z)\phi(z),\ \phi(z)^2]\mathrm{d}z, \tag{29}$$

$$\begin{aligned}&[\beta_7,\ \beta_8,\ \beta_9,\ \beta_{10}]\\ &= \int_{+t(x)/2-t_u}^{+t(x)/2} C_{55}^u \cos^2\theta_1 \sin^2\theta_1 [1,\ \chi(z),\ \chi(z)^2,\ \phi(z)]\mathrm{d}z,\end{aligned} \tag{30}$$

$$\begin{aligned}&[\beta_{11},\ \beta_{12}]\\ &= \int_{+t(x)/2-t_u}^{+t(x)/2} C_{55}^u \cos^2\theta_1 \sin^2\theta_1 [\chi(z)\phi(z),\ \phi(z)^2]\mathrm{d}z,\end{aligned} \tag{31}$$

$$\begin{aligned}&[\beta_{13},\ \beta_{14}]\\ &= \int_{+t(x)/2-t_u}^{+t(x)/2} [C_{11}^u,\ C_{55}^u]\left[\frac{\mathrm{d}\phi(z)}{\mathrm{d}z}\right]^2 \cos^2\theta_1 \sin^2\theta_1 \,\mathrm{d}z,\end{aligned} \tag{32}$$

$$[\beta_{15},\ \beta_{16}] = \int_{+t(x)/2-t_u}^{+t(x)/2} C_{55}^u \left[\frac{\mathrm{d}\phi(z)}{\mathrm{d}z}\right]^2 [\sin^4\theta_1,\ \cos^4\theta_1]\,\mathrm{d}z, \tag{33}$$

$$\begin{aligned}&[\beta_{17},\ \beta_{18},\ \beta_{19},\ \beta_{20}]\\ &= \int_{-t(x)/2}^{-t(x)/2+t_l} C_{11}^l \cos^4\theta_2 [1,\ \chi(z),\ \chi(z)^2,\ \phi(z)]\mathrm{d}z,\end{aligned} \tag{34}$$

$$[\beta_{21},\ \beta_{22}] = \int_{-t(x)/2}^{-t(x)/2+t_l} C_{11}^l \cos^4\theta_2 [\chi(z)\phi(z),\ \phi(z)^2]\mathrm{d}z, \tag{35}$$

$$\begin{aligned}&[\beta_{23},\ \beta_{24},\ \beta_{25},\ \beta_{26}]\\ &= \int_{-t(x)/2}^{-t(x)/2+t_l} C_{55}^l \cos^2\theta_2 \sin^2\theta_2 [1,\ \chi(z),\ \chi(z)^2,\ \phi(z)]\mathrm{d}z,\end{aligned} \tag{36}$$

$$\begin{aligned}&[\beta_{27},\ \beta_{28}]\\ &= \int_{-t(x)/2}^{-t(x)/2+t_l} C_{55}^l \cos^2\theta_2 \sin^2\theta_2 [\chi(z)g(z),\ \phi(z)^2]\mathrm{d}z,\end{aligned} \tag{37}$$

$$[\beta_{29}, \quad \beta_{30}] = \int_{-t(x)/2}^{-t(x)/2+t_l} [C_{11}^l, \quad C_{55}^l] \left[\frac{\mathrm{d}\phi(z)}{\mathrm{d}z}\right]^2 \cos^2\theta_2 \sin^2\theta_2 \, \mathrm{d}z, \tag{38}$$

$$[\beta_{31}, \quad \beta_{32}] = \int_{-t(x)/2}^{-t(x)/2+t_l} C_{55}^l \left[\frac{\mathrm{d}\phi(z)}{\mathrm{d}z}\right]^2 [\sin^4\theta_2, \quad \cos^4\theta_2] \, \mathrm{d}z, \tag{39}$$

$$[\beta_{33}, \quad \beta_{34}, \quad \beta_{35}, \quad \beta_{36}] = \int_{-t(x)/2+t_l}^{+t(x)/2-t_u} C_{11}^c [1, \quad \chi(z), \quad \chi(z)^2, \quad \phi(z)] \mathrm{d}z, \tag{40}$$

$$[\beta_{37}, \quad \beta_{38}] = \int_{-t(x)/2+t_l}^{+t(x)/2-t_u} C_{11}^c [\chi(z)\phi(z), \quad \phi(z)^2] \mathrm{d}z, \tag{41}$$

$$\beta_{39} = \int_{-t(x)/2+t_l}^{+t(x)/2-t_u} C_{55}^c \left[\frac{\mathrm{d}\phi(z)}{\mathrm{d}z}\right]^2 \mathrm{d}z \tag{42}$$

3. GDQ Method

To solve the governing differential equations accurately while minimizing CPU consumption, the GDQ technique has been chosen. The GDQ method is used to transform the differential equations into algebraic equations. To achieve this axial transformation, one can utilize the following approximations (Ghabussi *et al*. 2019, Mahinzare *et al*. 2024):

$$\frac{\mathrm{d}^n f_x(x_i)}{\mathrm{d}x^n} = \sum_{k=1}^{N} A_{ik}^{(n)} f(x_k) \ , \ n = 1, \ldots, N-1 \tag{43}$$

These weighting coefficients are denoted as $A_{ik}^{(n)}$. Here is the formula for the first-order weighting coefficient (Civalek 2004):

$$A_{ij}^{(1)} = \begin{cases} \dfrac{M(x_i)}{(x_i - x_j)M(x_j)} & \text{For Non-diagonal Arrays} \\ -\sum\limits_{\substack{j=1 \\ i \neq j}}^{N} A_{ij}^{(1)} & \text{For Diagonal Arrays} \end{cases} \tag{44}$$

that:

$$M(x_i) = \prod_{\substack{j=1 \\ j \neq i}}^{N} (x_i - x_j) \tag{45}$$

The subsequent equation can be employed to calculate higher-order weighting coefficients:

$$A_{ij}^{(n)} = n \left(A_{ii}^{(n-1)} A_{ij}^{(1)} - \frac{A_{ij}^{(n-1)}}{(x_i - x_j)} \right) \tag{46}$$

The reliability of the results is greatly affected by the dispersion of the grid points. A non-uniform axial distribution of nodes is generated in this study by using the roots of Chebyshev polynomials (Alhaifi *et al*. 2021):

$$x_i = \frac{a}{2}\left[1 - \cos\left(\frac{i-1}{N-1}\right)\pi\right], \ \ i = 1, \ldots, N \tag{47}$$

Given this setting, *N* is the sum of all grid points along the axial direction.

In the end, the relevant boundary conditions and the equilibrium equations can be used to generate the following matrix equation:

$$\left([K_e] + N^{cr}[K_g]\right)\begin{Bmatrix}\{d_b\} \\ \{d_d\}\end{Bmatrix} = 0 \tag{48}$$

The vectors $\{d_d\}$ and $\{d_b\}$ indicate the displacements inside and at the domain boundaries, the elastic stiffness and geometrical stiffness matrices are $[K_e]$ and $[K_g]$, and the critical buckling load is represented by N^{cr}. For the structure that is not yet evaluated, the critical buckling loads can be determined via non-trivial solutions to the most recent equation.

4. Results and discussion

4.1 Convergence study

The convergence of the results about the number of grid points will be addressed next. The critical buckling loads for different conditions based on number of grid points are obtained and also, are shown in Fig. 2. It can be observed that for different considered conditions such as buckling modes, length, and thickness change slope, as the quantity of grid points escalates, the results converge towards their definitive values, and at a particular threshold, the discrepancies between the outcomes become negligible. Consequently, a cumulative total of 17 points is employed to achieve the subsequent results.

4.2 Verification study

Before presenting the results, it is essential to evaluate their reliability. To attain this objective and in the absence of a comparable study, the results are compared with those from previously published research. To validate the previously proposed solution methodology and outcomes, it was implemented in the case study detailed in Refs. (Babaei *et al*. 2019, Ferreira 2009). In Table 1, a comparison of critical buckling load in the present study with Refs. (Babaei *t al*. 2019, Ferreira 2009) is provided for an isotropic single-layer constant thickness beam for two types of boundary conditions, namely both ends clamped and both ends simply supported. It is noteworthy that the following material properties and geometrical parameters are used to extract the results of Table 1: E=10MPa, a=1m, b=1m, ν=0.33. Table 1 demonstrates a significant correlation between the findings of the present study and those derived from the referenced literature. The results' accuracy and validity are confirmed. Consequently, the reliability of the formulations and the solution methodology is assured.

Consequently, the outcomes of the current research will

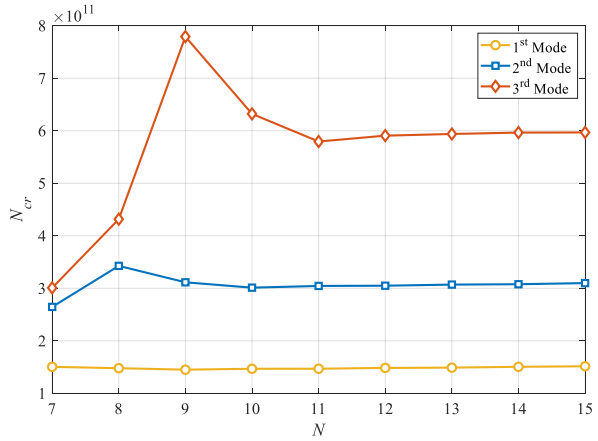

(a)

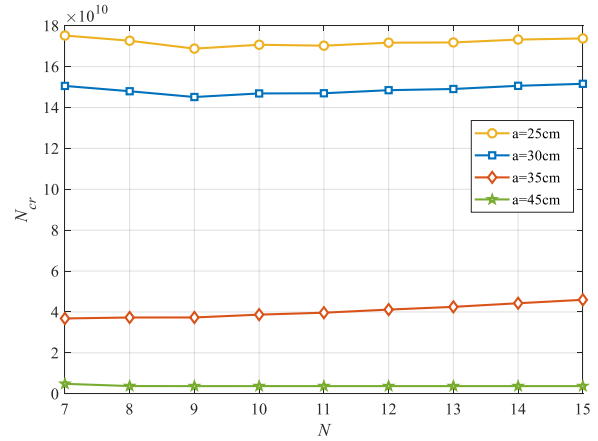

(b)

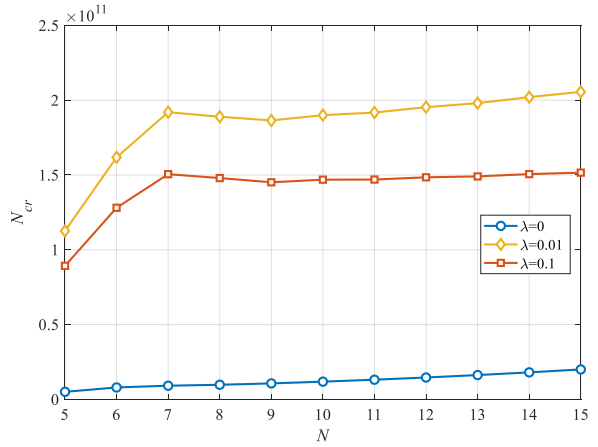

(c)

Fig. 2 Convergence study of the results

Table 1 Comparison of critical buckling load in the current study with Refs. (Babaei *et al.* 2019, Ferreira 2009).

B.C.	*a/t*	Current	Ferreira 2009	Babaei *et al.* 2019
C-C	10	29774	29766	29777
	100	32.865	32.864	32.865
	1000	0.0329	0.0329	0.0329
S-S	10	8014.18	8013.8	8014.4
	100	8.222	8.223	8.222
	1000	0.0082	0.0082	0.0082

Table 2 Material properties of the facesheets' constituents (Yadav *et al.* 2021)

Properties	CNTs	PMMA
v	0.175	0.34
$\rho\ (kg/m^3)$	1400	1150
$E_{11}\ (TPa)$	5.6466	$E_m\ (GPa)$= 3.52
$G_{12}\ (TPa)$	1.9445	

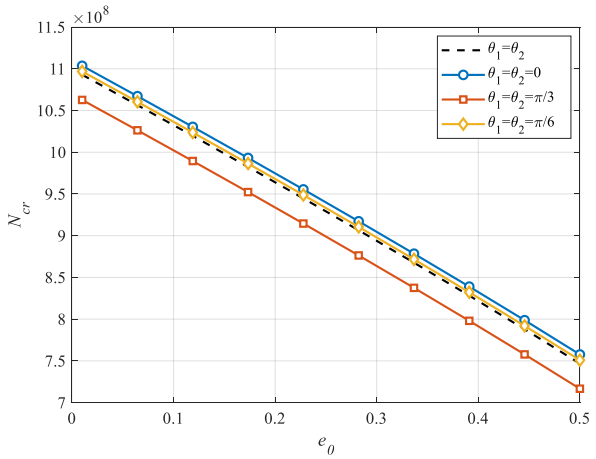

Fig. 3 The effect of porosity coefficient and rotation angle of the facesheets on the results

be presented in the subsequent subsection after verifying the reliability of the findings, their convergence, and the appropriate selection of grid points.

4.3 Parametric study

The findings of the present inquiry are delineated as follows. It is crucial to note that Table 2 enumerates the distinct material properties of the PMMA matrix and CNT reinforcement in the facesheets.

Furthermore, each volume fraction of CNTs possesses a unique set of efficiency characteristics, as delineated in Eq. (9). For $V_{CNT}^{*} = 0.12$ the efficiency parameters are as $\gamma_1 = 0.137$ and $\gamma_3 = 0.715$. For $V_{CNT}^{*} = 0.17$, they are as $\gamma_1 = 0.142$ and $\gamma_3 = 1.138$. Also, $\gamma_1 = 0.141$ and $\gamma_3 = 1.109$ are for $V_{CNT}^{*} = 0.28$. Furthermore, the foam utilized to create the FGC core possesses the subsequent mechanical specifications: E= 200GPa, ρ= 7850kg/m^3, v= 0.34.

Fig. 3 analyzes the impact of the rotation angle of facesheets and the porosity coefficient on critical buckling loads. It has been determined that, as anticipated, augmenting the rotation angle diminishes the critical buckling loads due to the increased flexibility of the beams. Moreover, Also, it can be seen that the critical buckling loads reduce by increasing the porosity coefficient. Porosity introduces voids or empty spaces within the core material, reducing its effective density and stiffness (Young's modulus). A weaker core material contributes less to the overall structural rigidity of the sandwich beam, leading to lower resistance to buckling. Also, in sandwich beams, the core provides shear stiffness and stabilizes the facesheets under compressive loading. A higher porosity reduces the

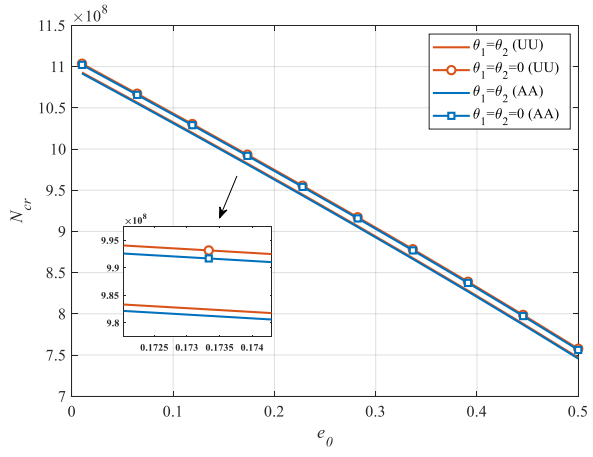

(a)

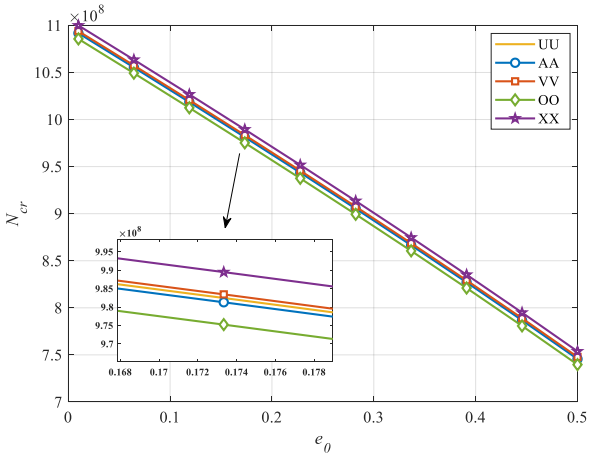

(b)

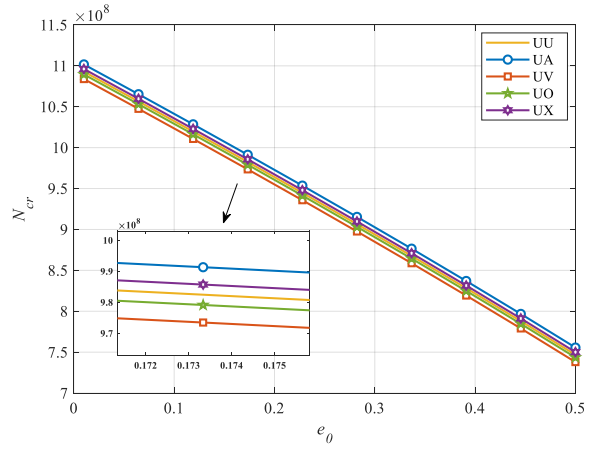

(c)

Fig. 4 Effect of porosity coefficient and CNTs distribution patterns on the results for different conditions

core's ability to distribute loads effectively, causing the facesheets to become more susceptible to local or global buckling. Moreover, the critical buckling load is proportional to the overall stiffness of the beam, which depends on both axial and shear stiffness. Increased porosity reduces the shear stiffness of the core, weakening the structure's resistance to out-of-plane deformations. Porosity can also lead to localized stress concentrations within the core, further exacerbating the reduction in load-

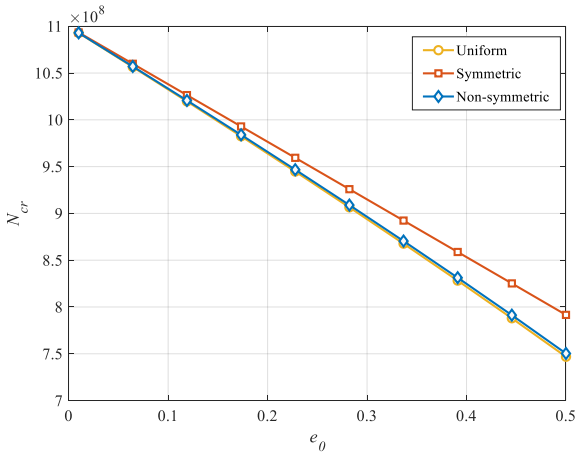

Fig. 5 Effect of porosity coefficient and pores distribution patterns on the results

bearing capacity and making the structure more prone to instability. As a conclusion, if the critical buckling load is expressed as a function of the effective stiffness of the core and the geometry of the sandwich beam, increasing the porosity coefficient decreases the core's stiffness (effective modulus). This results in a reduction of because is directly proportional to the stiffness.

Fig. 4 illustrates how CNTs distribution through the facesheets' thickness affects the critical buckling loads. The distribution of CNTs through the thickness of the facesheets significantly influences the critical buckling loads of the sandwich beam because it alters the mechanical properties (e.g., stiffness and strength) of the facesheets. FG CNT distribution patterns allow the tailoring of material properties to optimize the structural performance. Buckling resistance depends on the flexural rigidity, which is proportional to the material stiffness and the thickness distribution. CNT-rich outer surfaces in FG-XX configurations significantly enhance the flexural rigidity, increasing the critical buckling loads. Also, buckling occurs due to the instability of the compressive stress field. FG patterns like FG-XX reduce stress concentrations by reinforcing the regions of highest stress, thus delaying the onset of buckling. The choice of CNT distribution pattern directly impacts the critical buckling loads of the sandwich beam. FG-XX pattern is particularly effective in increasing the buckling resistance, as it strategically reinforces the areas of the facesheets most critical to stability under compressive loads. The selection of the pattern should be guided by the specific loading conditions and the intended application of the structure.

In Tables 3-6, the exact values of critical buckling loads for different conditions such as considering or neglecting rotation angle (CR and NR), slope variations, CNTs distribution patterns and mode numbers are listed that confirm the earlier findings in the figures.

The effect of porosity distribution patterns on the critical buckling loads is examined in detail in Fig. 5. The porosity distribution patterns in the core of a sandwich beam-whether uniform, symmetric, or nonsymmetric with respect to the mid-plane-play a critical role in determining the beam's structural response, including its critical buckling

Table 3 Effect of thickness variations slope, neglecting or considering rotation angle, and CNTs distribution patterns on the results ($\times 10^8$)

λ	UU		AA		VV		OO		XX	
	NR	CR	NR	CR	NR	CR	NR	CR	NR	CR
0.00	7.5148	7.3850	7.5155	7.3924	7.5138	7.3775	7.5138	7.3843	7.5156	7.3856
0.01	7.3784	7.3163	7.3786	7.3164	7.3780	7.3159	7.3805	7.3181	7.3761	7.3143
0.10	6.2142	6.2136	6.2083	6.2078	6.2177	6.2171	6.1638	6.1633	6.2636	6.2630
0.20	5.0510	4.6823	5.0362	4.6823	5.0571	4.6823	4.7863	4.6821	5.3076	4.6825

Table 4 Effect of neglecting or considering rotation angle and CNTs distribution patterns on the critical buckling loads of different modes for λ=0.1 ($\times 10^8$)

Buckling Mode	UU		AA		VV		OO		XX	
	NR	CR	NR	CR	NR	CR	NR	CR	NR	CR
First	0.6214	0.6214	0.6208	0.6208	0.6218	0.6217	0.6164	0.6208	0.6264	0.6263
Second	0.8779	0.8778	0.8772	0.8771	0.8783	0.8782	0.8700	0.8771	0.8856	0.8855
Third	1.2706	1.2705	1.2688	1.2687	1.2717	1.2716	1.2576	1.2687	1.2833	1.2832
Fourth	1.5730	1.5730	1.5716	1.5715	1.5740	1.5740	1.5645	1.5715	1.5817	1.5816

Table 5 Effect of neglecting or considering rotation angle and CNTs distribution patterns on the critical buckling loads of different modes for λ=0.2 ($\times 10^8$)

Buckling Mode	UU		AA		VV		OO		XX	
	NR	CR	NR	CR	NR	CR	NR	CR	NR	CR
First	0.5051	0.4682	0.5036	0.4682	0.5057	0.4682	0.4786	0.4682	0.5308	0.4682
Second	0.7108	0.6587	0.7089	0.6587	0.7112	0.6587	0.6697	0.6587	0.7495	0.6587
Third	1.0216	0.9467	1.0171	0.9467	1.0239	0.9467	0.9609	0.9467	1.0818	0.9468
Fourth	1.3365	1.2442	1.3329	1.2442	1.3390	1.2442	1.3081	1.2442	1.3740	1.2443

Table 6 Effect of neglecting or considering rotation angle and CNTs distribution patterns on the critical buckling loads ($\times 10^7$)

Upper layer	U		A		V		O	
Lower layer	NR	CR	NR	CR	NR	CR	NR	CR
A	5.1802	4.6824	-	-	-	-	-	-
V	4.9197	4.6822	4.7785	4.6821	-	-	-	-
O	4.9253	4.6822	4.7836	4.6821	5.0632	4.6823	-	-
X	5.1739	4.6824	5.0304	4.6823	5.3138	4.6825	5.0344	4.6823

loads. These patterns affect the stiffness, stress distribution, and load transfer efficiency of the core, ultimately influencing the beam's resistance to buckling under compressive loads. Uniform porosity is the simplest but least efficient pattern in terms of critical buckling loads. Symmetric porosity distribution is generally the most effective for improving buckling resistance under symmetric loading conditions. Nonsymmetric porosity distribution can be highly effective in specific scenarios but requires careful alignment with the loading and boundary conditions to avoid stress imbalances and instability.

In Tables 7 and 8, exact values of critical buckling loads for different patterns of pores' distribution across the core's thickness are listed versus porosity coefficient and also, the initial thickness. These tables also confirm the previous findings about the impact of the mentioned parameters on the critical buckling loads.

The impact of length-to-core's thickness of the under-examination beam for different geometrical and physical conditions on the elastic buckling performance of the model is shown in Fig. 6. It is observed that as the ratio of the beam's length-to-core's thickness increases, the results tend to reduction. The length-to-thickness ratio is a measure of the slenderness of the core. A higher ratio means the core becomes longer and thinner relative to its thickness, increasing its slenderness. Slender cores are less resistant to buckling because they are more prone to deformation under compressive loads. The critical buckling load is proportional to the flexural rigidity of the beam, which depends on the stiffness (Young's modulus) and the moment of inertia of the cross-section. As length-to-thickness ratio increases, the moment of inertia decreases

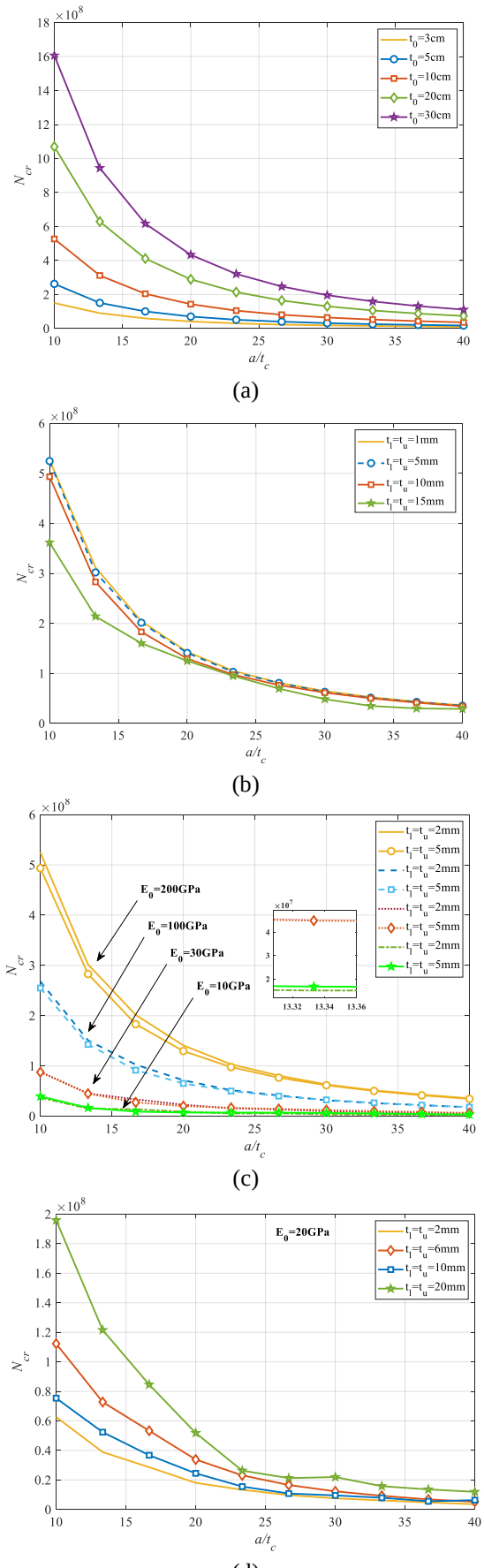

Fig. 6 Effect of geometrical parameters of the under-evaluation beam on the critical buckling loads

Table 7 Effect of porosity coefficient and pores distribution patterns on the critical buckling loads of different modes ($\times 10^7$)

e_0	Uniform	Symmetric	Non-symmetric
0.0	6.6118	6.6118	6.6118
0.1	6.2136	6.2529	6.2200
0.2	5.8070	5.8939	5.8193
0.3	5.3903	5.5350	5.4078

Table 8 Effect of initial thickness and pores distribution patterns on the critical buckling loads of different modes ($\times 10^8$)

t_0 (cm)	Uniform	Symmetric	Non-symmetric
2	0.0793	0.0783	0.0792
5	2.8890	0.6253	0.6220
10	1.7341	1.7645	1.7395
15	0.6214	2.9513	2.9002

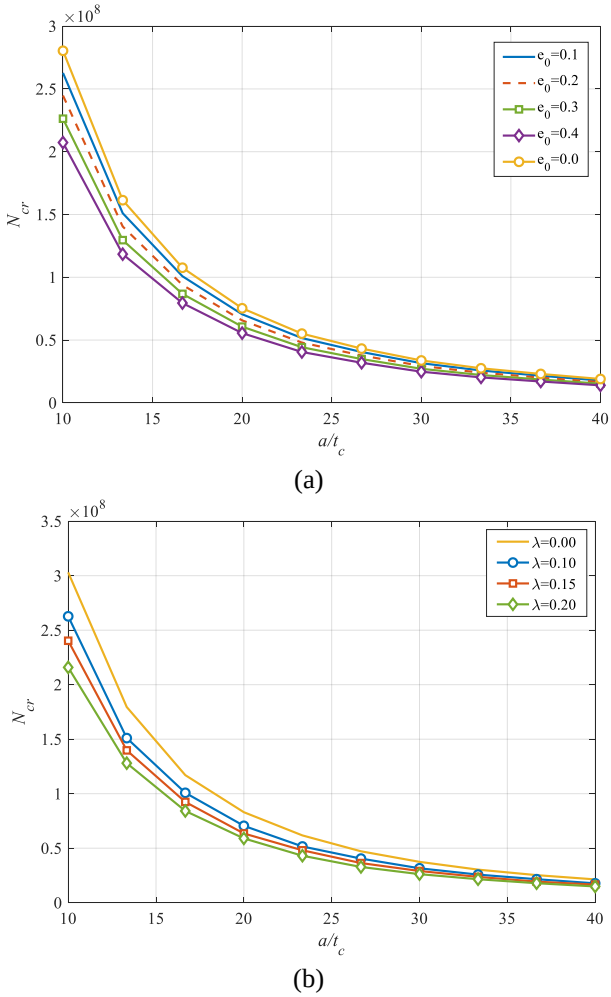

Fig. 7 Effect of thickness variations' slope on the results

significantly because it depends on the thickness cubed. This results in a lower flexural rigidity and thus reduces the critical buckling load. Also, in sandwich beams with a porous core, the core primarily resists shear deformation. A

Table 9 Effect of facesheets' thickness, neglecting or considering rotation angle, and CNTs distribution patterns on the critical buckling loads ($\times 10^7$)

t_l=t_u (mm)	UU		AA		VV		OO		XX	
	NR	CR	NR	CR	NR	CR	NR	CR	NR	CR
2	0.7709	0.7539	0.7691	0.7539	0.7717	0.7539	0.7167	0.7539	0.8238	0.7540
3	0.6729	0.6486	0.6712	0.6486	0.6736	0.6486	0.6283	0.6486	0.7164	0.6487
4	0.5845	0.5536	0.5829	0.5536	0.5851	0.5536	0.5492	0.5535	0.6188	0.5536
5	0.5051	0.4682	0.5036	0.4682	0.5057	0.4682	0.4786	0.4682	0.5308	0.4682

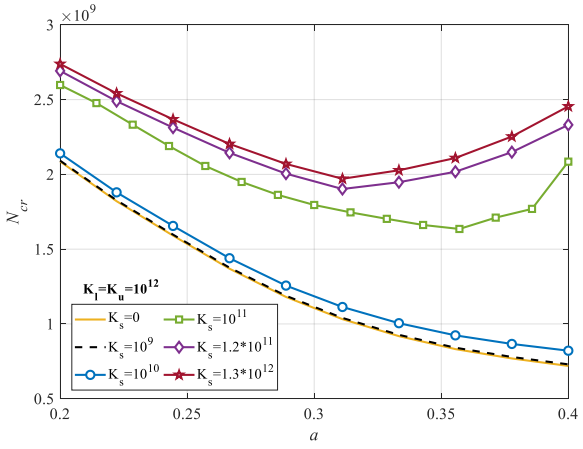

(a)

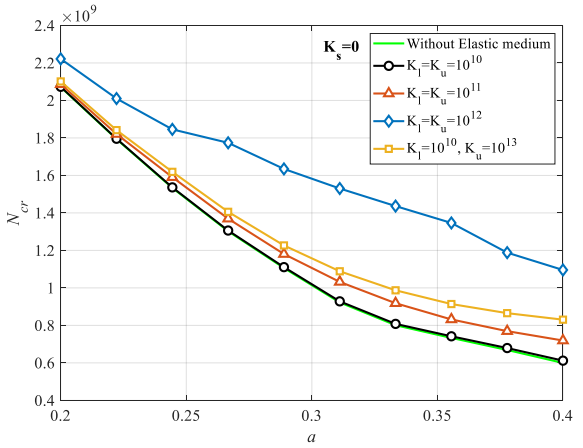

(b)

Fig. 8 Effect of thickness variations' slope on the results

thinner core (higher a/t) has reduced shear stiffness, which compromises the ability of the core to stabilize the facesheets under compressive loads. This reduction in shear stiffness further decreases the beam's ability to resist buckling.

The effect of different parameters such as rotation angle of facesheets, their thickness and also, CNTs' distribution pattern cross their thickness is considered in Table 9 and the values of critical buckling loads are listed in this table. This table also confirms the earlier findings.

The effect of different parameters such as rotation angle of facesheets, their thickness and also, CNTs' distribution pattern cross their thickness is considered in Table 9 and the values of critical buckling loads are listed in this table. This table also confirms the earlier findings.

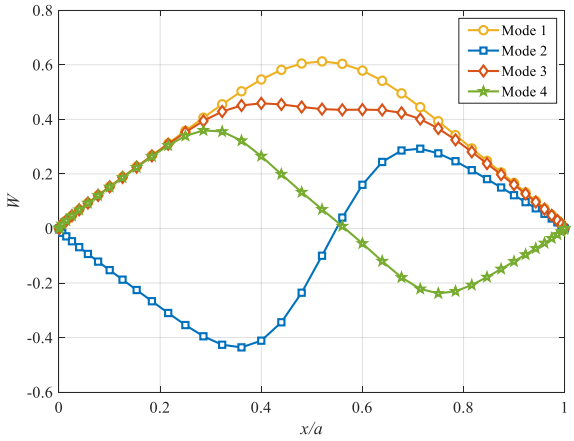

Fig. 9 Normalized deflection of the beam for the first four buckling modes

The effect of the porosity coefficient variations and also, and also slope of the thickness variation versus the beam's aspect ratio is investigated in Fig. 7. It is observed as the slope of thickness changes increases, the critical buckling loads reduce due to reduction in the whole beam's stiffness. The effects of Kerr elastic foundation parameters, i.e., shear layer parameter, upper and lower spring parameters on the results are shown in Fig. 8. It is seen that as these parameters increase, the critical buckling loads of the structure enhance due to enhancement in the model's rigidity.

5. Conclusions

A wide range of thickness profiles for sandwich beams are analyzed in this study to determine their elastic buckling behavior. The thickness of these beams gradually decreases as they are stretched out. The FGCMs make up the sandwich beams' core material, while the CNTs reinforce the facesheets. Because these reinforcements are distributed differently in relation to the height of the beam, it is necessary to perform stress transformations at specific angles in order to find the same material properties with precision. The equilibrium equations are formulated in this study using the variational method and the virtual displacement idea. The impacts of shape, porosity coefficient, different distribution patterns of porosity and CNTs, transformation angle, and other parameters on the critical buckling loads are thoroughly evaluated using GDQM, a robust numerical technique. The results indicate

that, as anticipated, increasing the rotation angle decreases the critical buckling loads due to the greater softening of the beams. Furthermore, it is evident that the critical buckling loads diminish with an increase in the porosity coefficient. The distribution of CNTs within the thickness of the facesheets greatly affects the critical buckling loads of the sandwich beam by modifying the mechanical properties, such as stiffness and strength, of the facesheets. CNT-rich outer surfaces markedly improve flexural stiffness, hence augmenting key buckling stresses. The porosity distribution patterns within the core of a sandwich beam—whether uniform, symmetric, or nonsymmetric relative to the mid-plane—are crucial in influencing critical buckling loads. These patterns influence the stiffness, stress distribution, and load transfer efficiency of the core, ultimately affecting the beam's resistance to buckling under compressive stresses. It is found that as the length-to-thickness ratio of the beam grows, the outcomes tend to diminish. Furthermore, it is noted that when the slope of thickness variations increases, the critical buckling loads diminish due to a decrease in the overall stiffness of the beam. As Kerr elastic foundation parameters' values increase, the critical buckling loads of the structure improve due to an increase in the model's stiffness.

References

Abazid, M.A., Zenkour, A.M. and Sobhy, M. (2020), "Wave propagation in FG porous GPLs-reinforced nanoplates under in-plane mechanical load and Lorentz magnetic force via a new quasi 3D plate theory", *Mech. Based Des. Struct.*, **50**(5), 1831-1850.. https://doi.org/10.1080/15397734.2020.1769651.

Ait Atmane, H., Tounsi, A. and Bernard, F. (2017), "Effect of thickness stretching and porosity on mechanical response of a functionally graded beams resting on elastic foundations", *Int. J. Mech. Mater. Des.*, **13**(1), 71-84. https://doi.org/10.1007/s10999-015-9318-x.

Alhaifi, K., Arshid, E. and Khorshidvand, A.R. (2021), "Large deflection analysis of functionally graded saturated porous rectangular plates on nonlinear elastic foundation via GDQM", *Steel Compos. Struct.*, **39**(6), 795-809. https://doi.org/10.12989/scs.2021.39.6.795.

Alian, A.R., El-Borgi, S. and Meguid, S.A. (2016), "Multiscale modeling of the effect of waviness and agglomeration of CNTs on the elastic properties of nanocomposites", *Comput. Mater. Sci.*, **117**, 195-204. https://doi.org/10.1016/j.commatsci.2016.01.029.

Arshid, E., Amir, S. and Loghman, A. (2021), "Bending and buckling behaviors of heterogeneous temperature-dependent micro annular/circular porous sandwich plates integrated by FGPEM nano-Composite layers", *J. Sandw. Struct. Mater.*, **23**(8), 3836-3877. https://doi.org/10.1177/1099636220955027.

Arshid, E., Ghorbani, M.A., Momeni Nia, M.J., Civalek, Ö. and Kumar, A. (2023), "Thermo-elastic buckling behaviors of advanced fluid-infiltrated porous shells integrated with GPLs-reinforced nanocomposite patches", *Mech. Adv. Mater. Struct.*, 1-17. https://doi.org/10.1080/15376494.2023.2251015.

Arshid, E., Amir, S., Loghman, A. and Civalek, Ö. (2024), "Aerodynamic stability and free vibration of fgp-reinforced nano-fillers annular sector microplates exposed to supersonic flow", *Thin Walled Struct.*, 111610. https://doi.org/10.1016/j.tws.2024.111610.

Arshid, E. and Khoddami Maraghi, Z. (2025), "Dynamic analysis of prismatic auxetic trigonometric rotating blades integrated by GNPs-reinforced layers", *Mech. Based Des. Struct.*, 1-28. https://doi.org/10.1080/15397734.2025.2527206.

Arshid, E., Maraghi, Z.K. and Civalek, Ö. (2025), "Variable-thickness higher-order sandwich beams with FG cellular core and CNT-RC patches: vibrational analysis in thermal environment", *Arch. Appl. Mech.*, **95**(1), 2. https://doi.org/10.1007/s00419-024-02716-0.

Attia, M.A. and Mohamed, S.A. (2020), "Thermal vibration characteristics of pre/post-buckled bi-directional functionally graded tapered microbeams based on modified couple stress Reddy beam theory", *Eng. Comput.*, **38**(3), 2079-2105. https://doi.org/10.1007/s00366-020-01188-4.

Babaei, M., Asemi, K. and Safarpour, P. (2019), "Buckling and static analyses of functionally graded saturated porous thick beam resting on elastic foundation based on higher order beam theory", *Iran. J. Mech. Eng. Transact. ISME*, **20**(1), 94-112.

Babaei, M., Kiarasi, F., Asemi, K., Dimitri, R. and Tornabene, F. (2022), "Transient thermal stresses in fg porous rotating truncated cones reinforced by graphene platelets", *Appl. Sci.*, **12**(8), 3932. https://doi.org/10.3390/app12083932.

Babaei, H., Zavari, S., Kaveh, A., Arshid, E. and Civalek, O. (2024), "Dynamic Response of Advanced Lightweight Porous Plates Integrated with Nanocomposite Face sheets Resting on Elastic Substrate", *Int. J. Struct. Stabil. Dyn.*, **25**(12), 2550132. https://doi.org/10.1142/S0219455425501329.

Bakhshi Khaniki, H. and Hosseini-Hashemi, S. (2017), "Dynamic transverse vibration characteristics of nonuniform nonlocal strain gradient beams using the generalized differential quadrature method", *Eur. Phys. J. Plus*, **132**(11), 500. https://doi.org/10.1140/epjp/i2017-11757-4.

Banhart, J. (2001), "Manufacture, characterisation and application of cellular metals and metal foams", *Prog. Mater. Sci.*, **46**(6), 559-632. https://doi.org/10.1016/S0079-6425(00)00002-5.

Bekkaye, T.H.L., Fahsi, B., Bousahla, A.A., Bourada, F., Tounsi, A., Benrahou, K.H., Tounsi, A. and Al-Zahrani, M.M. (2020), "Porosity-dependent mechanical behaviors of FG plate using refined trigonometric shear deformation theory", *Comput. Concr.*, **26**(5), 450. https://doi.org/10.12989/CAC.2020.26.5.439.

Cao, M., Qin, Y., Cao, X., Wang, S., Liu, J., Xu, S., Lin, Y., Cao, W. and He, C. (2025a), "Crack path competition and biomimetic toughening strategy in soda-lime glass: Experimental study and phase-field simulation", *Theor. Appl. Fract. Mech.*, **139**, 105092. https://doi.org/10.1016/j.tafmec.2025.105092.

Cao, Y., Chi, H., Zhu, Z., Fan, S., Zhang, Y., Tang, Y. and Hou, D. (2025b), "Multi-functional self-sensing electronic gasket for structural health monitoring of transportation pipelines", *Adv. Funct. Mater.*, **35**(20). https://doi.org/10.1002/adfm.202412634.

Cen, Q., Wang, X., Jiang, X., Liu, L. and Wu, Z. (2025), "Global yield surface construction of polymethacrylimide foam by an integrated approach combining nanoindentation, machine learning and microstructure-informed modeling", *Mater. Des.*, **257**, 114412. https://doi.org/10.1016/j.matdes.2025.114412.

Cho, J.R. (2024), "Comparison of mechanical behaviors between cracked functionally graded GPL- and CNT-reinforced composite plates", *Struct. Eng. Mech.*, **92**(6), 533-546. https://doi.org/10.12989/SEM.2024.92.6.533.

Civalek, Ö. (2004), "Application of differential quadrature (DQ) and harmonic differential quadrature (HDQ) for buckling analysis of thin isotropic plates and elastic columns", *Eng. Struct.*, **26**(2), 171-186. https://doi.org/10.1016/j.engstruct.2003.09.005.

Cui, Z., Yuan, Z. and Xi, C. (2024), "Engineering the future: Exploring the dynamic behavior of nanocomposite porous beams under the influence of nanoparticles", *Struct. Eng. Mech.*, **92**(5), 513-520.

https://doi.org/10.12989/SEM.2024.92.5.513.
Dawe, D.J. and Yuan, W.X. (2001), "Overall and local buckling of sandwich plates with laminated faceplates, Part I: Analysis", *Comput. Method Appl. Mech. Eng.*, **190**(40-41), 5197-5213. https://doi.org/10.1016/S0045-7825(01)00169-4.
Djilali, N., Bousahla, A.A., Kaci, A., Selim, M.M., Bourada, F., Tounsi, A., Tounsi, A., Benrahou, K.H. and Mahmoud, S.R. (2022), "Large cylindrical deflection analysis of FG carbon nanotube-reinforced plates in thermal environment using a simple integral HSDT", *Steel Compos. Struct.*, **42**(6), 779-789. https://doi.org/10.12989/SCS.2022.42.6.779.
Ebrahimi, F.M.V. (2019), "Vibration analysis of magneto-flexo-electrically actuated porous rotary nanobeams considering thermal effects via nonlocal strain gradient elasticity theory", *Adv. Nano Res.*, **7**(4), 223-231. https://doi.org/10.12989/anr.2019.7.4.223.
Eghbali, M. and Hosseini, S.A. (2024), "An accurate analytical exploration for dynamic response of thermo-electric CNTRC beams under driving harmonic and constant loads resting on Pasternak foundation ", *Adv. Nano Res.*, **16**(6), 549. https://doi.org/10.12989/ANR.2024.16.6.549.
Eltaher, M.A., Esen, I., Abdelrahman, A.A. and Abdraboh, A.M. (2024), "Dynamic response of FG carbon nanotubes nanoplates embedded in elastic media under moving point load ", *Adv. Nano Res.*, **17**(3), 257. https://doi.org/10.12989/ANR.2024.17.3.257.
Ferdosi, S.B. and Khorramabadi, R. (2025), "The buckling behavior of a symmetric plate with a functionally graded composition, incorporating shape memory alloy wires subjected to heat treatment", *Shape Memory Superelast.*, **11**(1), 5-18. https://doi.org/10.1007/S40830-025-00531-2/METRICS.
Ferreira, A.J.M. (2009), *MATLAB Codes for Finite Element Analysis*, **157**, Springer Netherlands. https://doi.org/10.1007/978-1-4020-9200-8.
Ghabussi, A., Ashrafi, N., Shavalipour, A., Hosseinpour, A., Habibi, M., Moayedi, H., Babaei, B. and Safarpour, H. (2019), "Free vibration analysis of an electro-elastic GPLRC cylindrical shell surrounded by viscoelastic foundation using modified length-couple stress parameter", *Mech. Based Des. Struct.*, **49**(5), 738-762. https://doi.org/10.1080/15397734.2019.1705166.
Hajmohammad, M.H., Zarei, M.S., Farrokhian, A. and Kolahchi, R. (2018), "A layerwise theory for buckling analysis of truncated conical shells reinforced by CNTs and carbon fibers integrated with piezoelectric layers in hygrothermal environment", *Adv. Nano Res.*, **6**(4), 299-321. https://doi.org/10.12989/ANR.2018.6.4.299.
He, Y.J. and She, G. (2024), "Nonlinear forced vibration of imperfect FG beams with hygro-thermal factor", *Struct. Eng. Mech.*, **92**(2), 163. https://doi.org/10.12989/SEM.2024.92.2.163.
Karami, B. and Shahsavari, D. (2019), "Nonlocal strain gradient model for thermal stability of FG nanoplates integrated with piezoelectric layers", *Smart Struct. Syst.*, **23**(3), 215-225. https://doi.org/10.12989/sss.2019.23.3.215.
Kaveh, A., Babaei, H., Zavari, S., Arshid, E. and Civalek, Ö. (2024), "Vibrational response of a sandwich microplate considering the impact of flexoelectricity and based on a novel porous-FGM formulation", *Mech. Based Des. Struct.*, 1-22. https://doi.org/10.1080/15397734.2024.2337913.
Khoddami Maraghi, Z., Amir, S. and Arshid, E. (2022), "On the natural frequencies of smart circular plates with magneto-rheological fluid core embedded between magnetostrictive patches on Kerr elastic substance", *Mech. Based Des. Struct.*, 1-18. https://doi.org/10.1080/15397734.2022.2156885.
Khoddami Maraghi, Z. and Arshid, E. (2024), "On the vibrational behavior of variable thickness FG porous beams with graphene-reinforced nanocomposite facesheets", *Acta Mechanica*, **235**(8), 5161-5185. https://doi.org/10.1007/s00707-024-03987-y.
Khorasani, M., Soleimani-Javid, Z., Arshid, E., Lampani, L. and Civalek, Ö. (2021), "Thermo-elastic buckling of honeycomb micro plates integrated with FG-GNPs reinforced Epoxy skins with stretching effect", *Compos. Struct.*, **258**, 1-28. https://doi.org/10.1016/j.compstruct.2020.113430.
Kiarasi, F., Babaei, M., Mollaei, S., Mohammadi, M. and Asemi, K. (2021), "Free vibration analysis of FG porous joined truncated conical-cylindrical shell reinforced by graphene platelets", *Adv. Nano Res.*, **11**(4), 380. https://doi.org/10.12989/ANR.2021.11.4.361.
Kumar, P. and Harsha, S.P. (2022), "Static and vibration response analysis of sigmoid function-based functionally graded piezoelectric non-uniform porous plate", *J. Intell. Mater. Syst. Struct.*, **33**(17), 2197-2227. https://doi.org/10.1177/1045389X221077433.
Liu, Y., Su, J., He, D., Hao, P., Liu, Y., Wang, Z. and Wang, T. (2025), "Analytical model for corrugated rolling of composite plates considering the shear effect", *J. Manuf. Proc.*, **134**, 1069-1081. https://doi.org/10.1016/j.jmapro.2025.01.025.
Liu, Z., Zhu, K., Wen, X. and Kumar, A. (2024), "Nonlinear vibration analysis of FG porous shear deformable cylindrical shells covered by CNTs-reinforced nanocomposite layers considering neutral surface exact position", *Adv. Nano Res.*, **17**(1), 73. https://doi.org/10.12989/ANR.2024.17.1.061.
Ma, Z. and Liu, T.J. (2025), "Fretting contact of FGPM coating-substrate system under cyclic torque based on laminated model", *J. Intell. Mater. Syst. Struct.*, **36**(13), 926-946. https://doi.org/10.1177/1045389X251352806.
Mahinzare, M., Rastgoo, A. and Ebrahimi, F. (2024), "On nonlinear vibration of piezo-electrically multiscale hybrid nanocomposite sandwich plate including an auxetic core based on HSDT", *Int. J. Struct. Stabil. Dyn.*, **24**(5). https://doi.org/10.1142/S021945542450069X.
Matouk, H., Bousahla, A.A., Heireche, H., Bourada, F., Bedia, E.A.A., Tounsi, A., Mahmoud, S.R., Tounsi, A. and Benrahou, K.H. (2020), "Investigation on hygro-thermal vibration of P-FG and symmetric S-FG nanobeam using integral Timoshenko beam theory", *Adv. Nano Res.*, **8**(4), 293-305. https://doi.org/10.12989/anr.2020.8.4.293.
Meng, W., Wang, J., Zhang, X., Huang, X., Gao, J. and Hou, L. (2025), "Study and prediction of overload/underload effect on fatigue performance of novel fiber metal laminates under two-stage loading", *J. Mater. Eng. Perform.*, 1-18. https://doi.org/10.1007/s11665-025-10999-9.
Mirjavadi, S.S., Forsat, M., Nia, A.F., Badnava, S., Hamouda, A.M.S., Mirjavadi, S.S., Forsat, M., Nia, A.F., Badnava, S. and Hamouda, A.M.S. (2020), "Nonlocal strain gradient effects on forced vibrations of porous FG cylindrical nanoshells", *Adv. Nano Res.*, **8**(2), 156. https://doi.org/10.12989/ANR.2020.8.2.149.
Moradi-Dastjerdi, R. and Behdinan, K. (2021), "Free vibration response of smart sandwich plates with porous CNT-reinforced and piezoelectric layers", *Appl. Math. Modell.*, **96**, 66-79. https://doi.org/https://doi.org/10.1016/j.apm.2021.03.013.
Moradi-Dastjerdi, R., Behdinan, K., Safaei, B. and Qin, Z. (2020), "Buckling behavior of porous CNT-reinforced plates integrated between active piezoelectric layers", *Eng. Struct.*, **222**. https://doi.org/10.1016/j.engstruct.2020.111141.
Mousavi, S.B., Amir, S., Jafari, A. and Arshid, E. (2021), "Analytical solution for analyzing initial curvature effect on vibrational behavior of PM beams integrated with FGP layers based on trigonometric theories", *Adv. Nano Res.*, **10**(3), 235-251. https://doi.org/10.12989/anr.2021.10.3.235.
Ninh, D.G., Ha, N.H., Long, N.T., Tan, N.C., Tien, N.D. and Dao, D.V. (2023), "Thermal vibrations of complex-generatrix shells made of sandwich CNTRC sheets on both sides and open/closed

cellular functionally graded porous core", *Thin Wall. Struct.*, **182**, 110161. https://doi.org/10.1016/j.tws.2022.110161.

Niu, S., Liu, X., Wang, C., Mu, W., Xu, W. and Wang, Q. (2025), "Breaking the trade-off between complexity and absorbing performance in metamaterials through intelligent design", *Small*, 2502828. https://doi.org/10.1002/smll.202502828.

Öner, E., Uzun Yaylacı, E. and Yaylacı, M. (2024), "Multi-method examination of contact mechanics in orthotropic layers under gravity", *Mech. Mater.*, **195**, 105036. https://doi.org/10.1016/j.mechmat.2024.105036.

Panah, M., Khorshidvand, A.R., Khorsandijou, S.M. and Jabbari, M. (2019), "Pore pressure and porosity effects on bending and thermal postbuckling behavior of FG saturated porous circular plates", **42**(9), 1083-1109. https://doi.org/10.1080/01495739.2019.1614502.

Patil, R., Joladarashi, S. and Kadoli, R. (2023), "Effect of porosity and viscoelastic boundary conditions on FG sandwich beams in thermal environment: Buckling and vibration studies", *Structures*, **56**, 105001. https://doi.org/10.1016/j.istruc.2023.105001.

Rajendran, S., Loganathan, R., Yaylaci, M., Yaylaci, E.U. and Özdemir, M.E. (2024), "Vibration of piezo-magneto-thermo-elastic FG nanobeam submerged in fluid with variable nonlocal parameter", *Adv. Nano Res.*, **16**(5), 489. https://doi.org/10.12989/ANR.2024.16.5.489.

Rasooli Jazi, F., Amir, S. and Arshid, E. (2024), "Vibration analysis of asymmetric sandwich rotating FG porous discs coated with agglomerated nanocomposite facesheets", *Arch. Civil Mech. Eng.*, **24**(4), 201. https://doi.org/10.1007/s43452-024-01009-1.

Ren, Z., Yang, Z., Mu, W., Liu, T., Liu, X. and Wang, Q. (2025), "Ultra-broadband perfect absorbers based on biomimetic metamaterials with dual coupling gradient resonators", *Adv. Mater.*, **37**(11). https://doi.org/10.1002/adma.202416314.

Sekban, D.M., Uzun Yaylacı, E., Özdemir, M.E., Öztürk, Ş., Yaylacı, M. and Panda, S.K. (2024), "Formability behavior of AH-32 shipbuilding steel strengthened by friction stir process", *Theor. Appl. Fract. Mech.*, **132**, 104485. https://doi.org/10.1016/j.tafmec.2024.104485.

Sekban, D.M., Yaylacı, E.U., Özdemir, M.E., Yaylacı, M. and Tounsi, A. (2025), "Investigating formability behavior of friction stir-welded high-strength shipbuilding steel using experimental, finite element, and artificial neural network methods", *J. Mater. Eng. Perform.*, **34**(6), 4942-4950. https://doi.org/10.1007/s11665-024-09501-8.

Selvamani, R., Ebrahimi, F., Yaylacı, M., Öztürk, Ş. and Yaylacı, E.U. (2024a), "Nonlinear poro-thermo-forced vibration in curved sandwich magneto-electro-elastic shells under hygrothermal environment", *Acta Mechanica*, **235**(9), 5489-5528. https://doi.org/10.1007/s00707-024-03994-z.

Selvamani, R., Thangamuni, P., Yaylacı, M., Emin Özdemir, M. and Yaylacı, E.U. (2024b), "Nonlinear vibration and parametric excitation of magneto-thermo elastic embedded nanobeam using homotopy perturbation technique", *ZAMM J. Appl. Math. Mech.*, **104**(12). https://doi.org/10.1002/zamm.202400525.

Shariati, A., Ghabussi, A., Habibi, M., Safarpour, H., Safarpour, M., Tounsi, A. and Safa, M. (2020), "Extremely large oscillation and nonlinear frequency of a multi-scale hybrid disk resting on nonlinear elastic foundation", *Thin Wall. Struct.*, **154**, 106840. https://doi.org/10.1016/j.tws.2020.106840.

Shen, X., Li, T., Xu, L., Kiarasi, F., Babaei, M. and Asemi, K. (2024), "Free vibration analysis of FG porous spherical cap reinforced by graphene platelet resting on Winkler foundation", *Adv. Nano Res.*, **16**(1), 26. https://doi.org/10.12989/ANR.2024.16.1.011.

Singh, P.P. and Azam, M.S. (2021), "Size dependent vibration of embedded functionally graded nanoplate in hygrothermal environment by Rayleigh-Ritz method", *Adv. Nano Res.*, **10**(1), 25-42. https://doi.org/10.12989/ANR.2021.10.1.025.

Soleimani-Javid, Z., Arshid, E., Khorasani, M., Amir, S. and Tounsi, A. (2021), "Size-dependent flexoelectricity-based vibration characteristics of honeycomb sandwich plates with various boundary conditions", *Adv. Nano Res.*, **10**(5), 449-460. https://doi.org/10.12989/anr.2021.10.5.449.

Sorokin, S.V., Grishina, S.V. and Ershova, O.A. (2001), "Analysis and control of vibrations of honeycomb plates by parametric stiffness modulations", *Smart Mater. Struct.*, **10**(5), 1031-1045. https://doi.org/10.1088/0964-1726/10/5/320.

Sun, M., Qiu, Z., Chen, Q., Lei, H., Zhang, Z., Song, Y., Jiang, S., Zhao, J. and Fu, H. (2025), "A mechanical metamaterial for energy absorption using carbon fiber composite", *Int. J. Mech. Sci.*, **295**, 110282. https://doi.org/10.1016/j.ijmecsci.2025.110282.

Tahir, S.I., Chikh, A., Tounsi, A., Al-Osta, M.A., Al-Dulaijan, S.U. and Al-Zahrani, M.M. (2021), "Wave propagation analysis of a ceramic-metal functionally graded sandwich plate with different porosity distributions in a hygro-thermal environment", *Compos. Struct.*, **269**, 114030. https://doi.org/10.1016/j.compstruct.2021.114030.

Tang, H., Peng, J., Peng, H., Yang, Y., Gao, Q., Xiao, L., Li, H., Zheng, L., Chen, Z. and Yang, Z. (2025), "Test and theoretical investigations on flexural behavior of high-performance h-shaped steel beam with local corrosion in pure bending zone", *Steel Res. Int.*, **96**(7). https://doi.org/10.1002/srin.202400640.

Thang, P.T., Nguyen-Thoi, T., Lee, D., Kang, J. and Lee, J. (2018), "Elastic buckling and free vibration analyses of porous-cellular plates with uniform and non-uniform porosity distributions", *Aerosp. Sci. Technol.*, **79**, 278-287. https://doi.org/10.1016/j.ast.2018.06.010.

Turan, M., Kahya, V., Yaylacı, E.U. and Yaylacı, M. (2025), "A shear deformable numerical approaches for the static analysis of bi-directional functionally graded beams", *Adv. Nano Res.*, **18**(2), 143-162. https://doi.org/10.12989/ANR.2025.18.2.143.

Turan, M., Uzun Yaylacı, E. and Yaylacı, M. (2023), "Free vibration and buckling of functionally graded porous beams using analytical, finite element, and artificial neural network methods", *Arch. Appl. Mech.*, **93**(4), 1351-1372. https://doi.org/10.1007/s00419-022-02332-w.

Van Quyen, N., Van Thanh, N., Quan, T.Q. and Duc, N.D. (2021), "Nonlinear forced vibration of sandwich cylindrical panel with negative Poisson's ratio auxetic honeycombs core and CNTRC face sheets", *Thin Wall. Struct.*, **162**, 107571. https://doi.org/10.1016/j.tws.2021.107571.

Wang, Q., Ren, Z., Shi, L., Huang, Z., Feng, S. and Li, S. (2025), "Hysteresis characteristics of entangled porous metallic pseudo-rubber under complex topological structures and thermo-mechanical coupling effects", *Eur. J. Mech. A Solids*, **111**, 105597. https://doi.org/10.1016/j.euromechsol.2025.105597.

Xia, L., Wang, R., Chen, G., Asemi, K. and Tounsi, A. (2023), "The finite element method for dynamics of FG porous truncated conical panels reinforced with graphene platelets based on the 3-D elasticity", *Adv. Nano Res.*, **14**(4), 375. https://doi.org/10.12989/.2023.14.4.375.

Yadav, A., Amabili, M., Panda, S.K., Dey, T. and Kumar, R. (2021), "Nonlinear damped vibrations of three-phase CNT-FRC circular cylindrical shell", *Compos. Struct.*, **255**, 112939. https://doi.org/10.1016/j.compstruct.2020.112939.

Yao, S., Chen, Y., Sun, C., Zhao, N., Wang, Z. and Zhang, D. (2024), "Dynamic response mechanism of thin-walled plate under confined and unconfined blast loads", *J. Marine Sci. Eng.*, **12**(2), 224. https://doi.org/10.3390/jmse12020224.

Yaylacı, M., Yazıcıoğlu, A., Yaylacı, E.U., Terzi, M. and Birinci, A. (2025), "Evaluation of the contact problem of two layers one of functionally graded, loaded by circular rigid block and resting on a Pasternak foundation by analytical and numerical

(FEM and MLP) methods", *Arch. Appl. Mech.*, **95**(4), 78. https://doi.org/10.1007/s00419-025-02787-7.

Zenkour, A.M. and El-Shahrany, H.D. (2021), "Hygrothermal forced vibration of a viscoelastic laminated plate with magneto-strictive actuators resting on viscoelastic foundations", *Int. J. Mech. Mater. Des.*, **17**(2), 301-320. https://doi.org/10.1007/s10999-020-09526-6.

CC